Electrochimica Acta 235 (2017) 471–479

Contents lists available at ScienceDirect

Electrochimica Acta

journal homepage: www.elsevier.com/locate/electacta

Electrochemical performance of $Ti_3C_2T_x$ MXene in aqueous media: towards ultrasensitive H_2O_2 sensing

Lenka Lorencova[a,1], Tomas Bertok[a,1], Erika Dosekova[a], Alena Holazova[a], Darina Paprckova[a], Alica Vikartovska[a], Vlasta Sasinkova[a], Jaroslav Filip[b,2], Peter Kasak[b,*], Monika Jerigova[c,d], Dusan Velic[c,d], Khaled A. Mahmoud[e], Jan Tkac[a,*]

[a] Institute of Chemistry, Slovak Academy of Sciences, Dubravska cesta 9, Bratislava 845 38, Slovak Republic
[b] Center for Advanced Materials, Qatar University, P.O. Box 2713, Doha, Qatar
[c] Department of Physical Chemistry, Faculty of Natural Sciences, Comenius University, Mlynska Dolina, Bratislava, 84215, Slovak Republic
[d] International Laser Centre, Ilkovičova 3, Bratislava 84104, Slovak Republic
[e] Qatar Environment and Energy Research Institute (QEERI), Hamad Bin Khalifa University (HBKU), P.O. Box 5825, Doha, Qatar

ARTICLE INFO

Article history:
Received 21 January 2017
Received in revised form 8 March 2017
Accepted 9 March 2017
Available online 11 March 2017

Keywords:
$Ti_3C_2T_x$
H_2O_2 sensing
oxygen reduction reactions
NADH oxidation

ABSTRACT

An extensive characterization of pristine and oxidized $Ti_3C_2T_x$ (T: =O, —OH, —F) MXene showed that exposure of MXene to an anodic potential in the aqueous solution oxidizes the nanomaterial forming TiO_2 layer or TiO_2 domains with subsequent TiO_2 dissolution by F^- ions, making the resulting nanomaterial less electrochemically active compared to the pristine $Ti_3C_2T_x$. The $Ti_3C_2T_x$ could be thus applied for electrochemical reactions in a cathodic potential window i.e. for ultrasensitive detection of H_2O_2 down to nM level with a response time of ~10 s. The manuscript also shows electrochemical behavior of $Ti_3C_2T_x$ modified electrode towards oxidation of NADH and towards oxygen reduction reactions.

© 2017 Elsevier Ltd. All rights reserved.

1. Introduction

2D nanomaterials with a high specific surface area have a variety of promising properties, making them useful as carriers, novel electronic materials and as a part of optical devices, sensors and energy storage devices [1–4]. Since the description of properties of the first 2D nanomaterial – graphene in 2004 [5], there is an explosion of papers describing other 2D nanomaterials [6–10].

In 2011, a new family of 2D MXene nanomaterials were introduced [11], exhibiting more complex (layered) structure compared to graphene, having many specific properties, like metallic conductivity and hydrophilicity due to presence of a negative charge on the surface [12–14]. MXenes belong to a family of exfoliated transition metal carbides and carbonitrides synthesized by hydrofluoric acid (HF) etching of the "A" group element from "MAX" phase powders [15] (where "M" is a transition metal, "A" is an element mostly from groups 13 and 14 of a periodic table, and "X" is a carbon or a nitrogen atom [16]) resulting in 2D layered structure similar to graphenes [17].

The as-obtained MXene sheets are terminated with oxygen- and/or fluorine-containing functional groups (=O, —OH, —F). However, alkalization and calcination post-treatments were shown to remove these surface groups, thus enhancing electrical conductivity of the nanomaterial [18]. Up to now, the most common applications of MXenes are high capacity electrode materials for batteries [19–25], as supercapacitors [26] and pseudocapacitive cathode materials [27,28] or as an electromagnetic interference shielding material [4]. Environmental removal of Pb(II) ions using this nanomaterial was also reported [29]. $Ti_3C_2T_x$ in a colloidal solution exhibits an antimicrobial activity, which is higher compared to graphene oxide (GO) [30]. An adsorption and a photocatalytic decomposition of organic molecules in aqueous solutions were observed, as well [31].

From a sensing point of view, Ti_3C_2 either in a pristine form [32] or combined with TiO_2 nanoparticles [33] was shown to provide an excellent immobilization matrix for hemoglobin-based mediator-free biosensor for H_2O_2 detection with a limit of detection (LOD)

* Corresponding authors.
E-mail addresses: peter.kasak@qu.edu.qa (P. Kasak), Jan.Tkac@savba.sk (J. Tkac).
[1] These authors contributed equally.
[2] Current address: Department of Environment Protection Engineering, Tomas Bata University in Zlin, Vavreckova 275, Zlin 762 72, Czech Republic

http://dx.doi.org/10.1016/j.electacta.2017.03.073
0013-4686/© 2017 Elsevier Ltd. All rights reserved.

down to 14 nM and an excellent biosensor stability [33]. The same platform was also used to investigate detection of $NaNO_2$ with LOD of 120 nM [34]. The most recent study suggests immobilization of glucose oxidase on $Ti_3C_2T_X$ MXene modified by gold nanoparticles as a biointerface for sensitive detection of glucose [35]. Also, an adsorption of different gases (NH_3, H_2, CH_4, CO, CO_2, N_2, NO_2 and O_2) on Ti_2CO_2 monolayer was studied, resulting in an adsorption of only NH_3 molecules, making this material applicable not only as a battery material, but also as a potential gas sensor and NH_3 capturer with a high selectivity [36]. The most recent study described application of MXene patterned field-effect transistor for probing neural activity by detection of dopamine [37].

In this study, we focused on investigation of electrochemical performance of $Ti_3C_2T_X$ in an aqueous solution for potential sensing applications. $Ti_3C_2T_X$ was investigated for its ability to detect oxygen and hydrogen peroxide and to oxidize NADH, for potential future construction of biosensors. $Ti_3C_2T_X$ modified electrode proved to be extremely sensitive for detection of H_2O_2 with LOD of 0.7 nM. Detection of H_2O_2 as an analyte is of importance in chemical and food industry (applied as an oxidizing agent) and for detection in clinical, pharmaceutical and environmental samples (see an excellent paper reviewing construction of H_2O_2 sensors [38]). Furthermore, H_2O_2 is a byproduct of enzymatic action of various oxidases so efficient detection of H_2O_2 is very important for development of oxidase-based biosensors utilizable in numerous applications [39–42].

2. Materials and methods

2.1. Materials

All chemicals (i.e. $K_3[Fe(CN)_6]$, $K_4[Fe(CN)_6]\cdot 3H_2O$, H_2O_2, H_2SO_4, NADH, NaOH, DMSO) and phosphate buffer (PB) components (KH_2PO_4 and K_2HPO_4, pH 7.0), were of ≥99% purity or p.a. grade and were purchased from Sigma Aldrich (USA). 50 wt% HF was obtained from Fisher Scientific, USA. All solutions were freshly prepared in 0.055 μS ultrapure deionized water (DW) and filtered *prior* use using 0.2 μm sterile filters.

2.2. $Ti_3C_2T_x$ MXene synthesis

Ti_3AlC_2 was synthesized as described previously [43]. Multilayer Ti_3C_2 MXene was prepared by HF treatment protocol with a minor modification. Briefly, Ti_3AlC_2 was added slowly to an aqueous HF solution (50 wt%) for 18 h at room temperature followed by intercalation with DMSO. The reaction mixture was washed several times with DW until pH 6 was reached. The colloidal solution of delaminated $Ti_3C_2T_x$ dispersion was obtained by sonication of $Ti_3C_2T_x$ powders (1 mg) in 2 mL of DW water, which was purged with argon for 60 min *prior* sonication, followed by centrifugation of the dispersion at 3,000 rpm for 1 h with a final collection of the supernatant.

2.3. Electrochemical procedures

All electrochemical procedures were run on a laboratory potentiostat/galvanostat Autolab PGSTAT 302N with an impedimetric module (Ecochemie, Utrecht, Netherlands) with a glassy carbon electrode (GCE, d = 3 mm, Bioanalytical systems, USA) used as a working electrode. Chronoamperometric detection of H_2O_2 at 300 rpm was performed on a rotating disc electrode employed as a working electrode. An Ag/AgCl/3 M KCl reference electrode and a counter Pt electrode (Bioanalytical systems, USA) were applied in a three-electrode cell system. Measurements were run under Nova Software 1.10, and data acquired were evaluated using OriginPro 9.1.

Chronoamperometry was applied as a useful method for determination of real surface area of $Ti_3C_2T_x$ modified GCE, which was calculated from a Cottrell equation:

$$i = \frac{nFAc_j^0\sqrt{D_j}}{\sqrt{\pi t}} \quad (1)$$

where n is the number of electrons exchanged, F is a Faraday constant (96,485 C mol^{-1}), c^o_j is concentration of the electrochemical mediator i.e. ferricyanide (mol cm^{-3}), D is the diffusion coefficient (7.6 10^{-6} cm^2 s^{-1} for ferricyanide solution used in this study), t is time (in s) and A is the real surface area (in cm^2). The experiment was conducted by applying two potentials (0.2 V and −0.6 V, respectively) for the reduction of 1 mM ferricyanide solution in 0.2 M KCl. Under diffusion control, a plot of i *vs.* $t^{-1/2}$ is linear and from the slope, the value of A could be obtained. Real surface area of $Ti_3C_2T_x$ modified GCE was 13.3 mm^2, while a geometric surface area of GCE was 7.1 mm^2.

Electrochemical impedance spectroscopy (EIS) can provide characteristics of an interfacial layer using a redox probe. The result of EIS analysis is presented in a Nyquist plot, from which such characteristics can be obtained. EIS was measured in an electrolyte containing 5 mM potassium hexacyanoferrate (III), 5 mM potassium hexacyanoferrate (II) and 0.1 M PB, pH 7.0. The analysis was run at 50 different frequencies (ranging from 0.1 Hz up to 100 kHz) under Nova Software 1.10 (Ecochemie, Netherlands). The results were presented in a form of a Nyquist plot, with an equivalent circuit R(Q[RW]) applied for data fitting.

2.4. Electrode modifications

First, the GCE was polished with a 1.0 μm alumina slurry and diamond polishing paste and sonicated in DW. The cleaned GCE was subsequently dried using a purified nitrogen stream. In order to obtain homogeneous $Ti_3C_2T_x$ dispersion, $Ti_3C_2T_x$ solution was sonicated for 1 min, if not specified otherwise, under Ar atmosphere to prevent potential oxidation of MXene. The $Ti_3C_2T_x$ modified electrode was prepared by a simple drop-casting method. The final volume of 30 μL of a MXene dispersion was pipetted on the GCE in two steps (2 × 15 μL) and allowed to dry at room temperature in a laminar box.

2.5. Preparation of oxidized $Ti_3C_2T_x$ ($oTi_3C_2T_x$)

Oxidation of $Ti_3C_2T_x$ was performed in 0.1 M PB pH 7.0 by a linear sweep voltammetry (LSV) running from 0 mV to 500 mV at a sweep rate of 100 mV s^{-1}.

2.6. Characterization of $Ti_3C_2T_x$ and $oTi_3C_2T_x$

Raman spectra were measured with a DXR Raman Microscope (Thermo Scientific, USA) with 532 nm laser in the region from 3,350 to 52 cm^{-1} (laser power 0.5 mW, exposure time 20 s, number of exposures 10, slit: 50 μm).

Contact angle measurements were run on a portable instrument System E (Advex Instruments, Czech Republic) to reveal contact angle and free surface energy for $Ti_3C_2T_x$ modified interfaces. The droplet volume was 2 μL and the testing liquid was distilled water. Free surface energy was determined using the two-liquid Owens-Wendt (OW) method, where the total surface energy γ consists of disperse γ^d and polar γ^p components. Water and diiodomethane were used as test liquids (surface tension values according to Strom). In order to minimize measurement error, 5 contact angles were measured, with the highest and the lowest value eliminated. For each sample, the water and

diiodomethane contact angle was obtained as an average value of assays performed using 3 droplets.

A peak force tapping mode atomic force microscopy (AFM, Scan Asyst, Bruker, USA) in air was carried out on a Bioscope Catalyst instrument and Olympus IX71 microscope in conjunction with NanoScope 8.15 software at a scan rate of 0.5 line s^{-1} with the tip set automatically for optimal gain. AFM mica substrates (grade V-1, d = 12 mm, SPI Supplies, USA) modified with $Ti_3C_2T_x$ were scanned using a SCANASYST-AIR silicon tip on a nitride lever (Bruker, USA, with f_0 = 50–90 kHz and k = 0.4 N m^{-1}), sharpened to a tip radius of 2 nm.

The same modified substrates i.e. modified square shaped gold chips (Arrandee, Germany) as for AFM imaging were applied for obtaining scanning electron microscopy (SEM) images using Carl Zeiss EVO 40HV apparatus (Germany) after Au CVD treatment to observe the structure of $Ti_3C_2T_x$.

XPS signals for $Ti_3C_2T_x$ and o$Ti_3C_2T_x$ were recorded on modified square shaped Au chips (Arrandee, Germany) using a Thermo Scientific K-Alpha XPS system (Thermo Fisher Scientific, UK) equipped with a micro-focused, monochromatic Al K alpha X-ray source (1486.6 eV). An X-ray beam of 400 μm size was used at 6 mA × 12 kV. The spectra were acquired in the constant analyzer energy mode with pass energy of 200 eV for the survey. Narrow regions were collected with pass energy of 50 eV. Charge compensation was achieved with the system flood gun that provides low energy electrons (~0 eV) and low energy argon ions (20 eV) from a single source. The argon partial pressure was 2×10^{-7} mbar in the analysis chamber. The Thermo Scientific Avantage software, version 4.84 (Thermo Fisher Scientific), was used for digital acquisition and data processing. Spectral calibration was determined using the automated calibration routine and the internal Au, Ag and Cu standards supplied with the K-Alpha system. The surface compositions (in atomic %) were determined by considering the integrated peak areas of atoms and the respective sensitivity factors.

$Ti_3C_2T_x$ was further characterized using X-Ray powder diffraction (XRD) measurements to investigate crystal structure of the material. Typical samples were prepared by pipetting of 20 μL of $Ti_3C_2T_x$ dispersion (1.5 mg mL^{-1} in DW, sonication for 30 min unless stated otherwise) on a glass slide, dried under reduced pressure, gently rinsed with DW to wash out any particles not incorporated into the formed $Ti_3C_2T_x$ film and dried in Ar stream. The samples were characterized using XRD equipment Empyrean with irradiation source Cu Kα1 (λ=0.15406 nm) at tension 45 kV and current 40 mA and detector PIXcel1D with stage platform with adjustable Z-height (all from PANalaytical). Value of Z-height was determined for each sample using micrometer. X-ray diffraction was observed in gonio mode in 2θ range of 4°–20° with step size 0.0066° and scan speed 0.055° s^{-1}. Size of the main lattice distance (d) corresponds to the peak position, i.e. to the angle of the diffracted beam, according to the Bragg's law λ = 2d sin θ, where λ is 0.15406 nm and sinθ was calculated from the position 2θ of the given XRD peak. The domain size can be calculated using Scherrer formula s = K λ/β cosθ where s, K and β stands for a mean domain size, a shape factor (0.9) and a broadness of the peak in half its maximum intensity (FWHM) in radians, respectively.

Secondary Ion Mass Spectrometry (SIMS) is a technique for sensitive chemical surface analysis of samples [44]. The analysis is not limited by the origin or type of a sample, that can be substantially any, inorganic, organic and biological. SIMS employing Time-of-Flight (TOF) analyzer provides elemental, chemical state and molecular information from surface layers or thin film structures with high sensitivity on the level of ppm-ppb. Besides, TOF SIMS IV spectrometers could provide high mass resolution, lateral resolution of 100 nm and a depth resolution of 1 nm. With the primary ion beam scanning across the sample surface, even the 2D chemical imaging of elements or molecules can be obtained providing data on a spatial distribution of predefined species [44]. Mass spectrometry measurements were performed using a TOF-SIMS IV (ION-TOF, Muenster, Germany), a reflectron type of time-of-flight mass spectrometer equipped with a Bismuth ion source. Pulsed 25 keV Bi^+ were used as primary ions with ion current of 1.1 pA. The TOF-SIMS spectra were measured by scanning over the 100 μm × 100 μm analysis area with a total primary ion dose density below the static limit of 10^{13} ions cm^{-2}. SIMS images were measured by scanning over the 200 μm × 200 μm analysis area, with a lateral resolution of 5 μm. All assays were performed in a positive and a negative polarity.

3. Results and discussion

3.1. Microscopic characterization of $Ti_3C_2T_x$ modified GCE

SEM images revealed formation of aggregates on the surface differing in size i.e. having few μm in size (Fig. 1 **left**) or with size larger than 10 μm (Fig. 1 **right**).

3.2. Electrochemical oxidation of $Ti_3C_2T_x$ (preparation of o$Ti_3C_2T_x$)

Initial cyclic voltammetry (CV) experiments confirmed that an anodic oxidation of $Ti_3C_2T_x$ is an irreversible process with an anodic peak appearing only in the first CV scan at a potential of 430 mV and could not be observed in the subsequent CV scans (Fig. 2). Further experiments revealed that this anodic peak

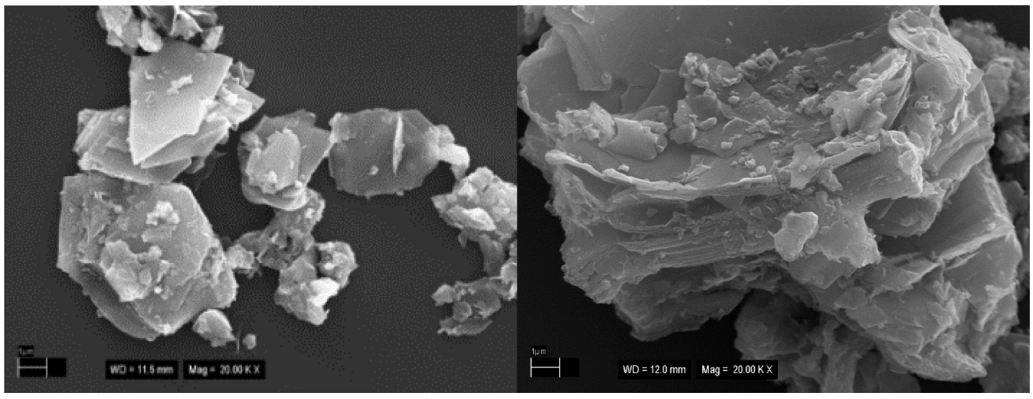

Fig. 1. Representative SEM images of $Ti_3C_2T_x$ sonicated for 1 min. Magnification: 20,000×.

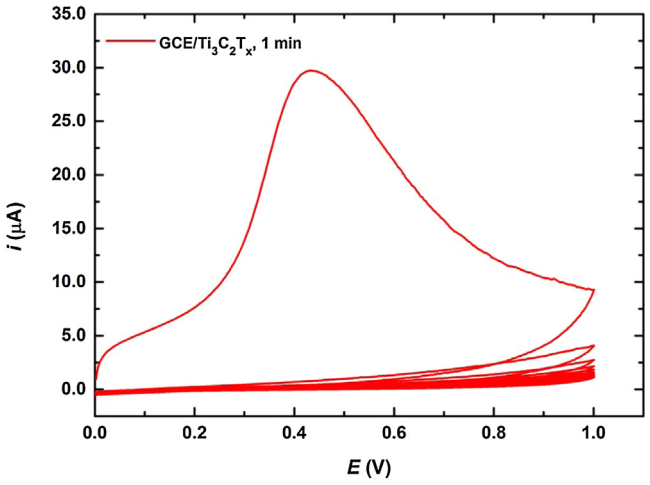

Fig. 2. CV of GCE/$Ti_3C_2T_x$ showing several consecutive scans run in a potential window from 0 V to 1 V at a sweep rate of 100 mV s^{-1} in 0.1 M PB pH 7.0. $Ti_3C_2T_x$ dispersion was prepared by 1 min sonication. Further details are provided in the Experimental section.

appeared only once and could not be seen if the $Ti_3C_2T_x$ modified GCE was further reduced by running CV in the potential window from 0 mV to −500 mV (as shown in Fig. 3), from −500 mV to −1,000 mV (data not shown) or after the $Ti_3C_2T_x$ modified GCE electrode was kept at an open circuit potential for couple of minutes. This really indicates irreversible oxidation of $Ti_3C_2T_x$ upon exposure to an anodic potential, which could not be re-reduced.

Optimization of sonication time for preparation of $Ti_3C_2T_x$ dispersions was performed also electrochemically either by running CV in the potential window from 0 mV to − 500 mV (Fig. 3) or in the potential window from 0 mV to 1,000 mV (Fig. S1). Such CV experiments confirmed that optimal sonication time for preparation of $Ti_3C_2T_x$ dispersion was 1 min. An increase of sonication time from 1 min to 10 min led to decrease of a Faradaic current (Fig. S1) or a capacitive current (Fig. 3). Sonication time longer than 10 min (up to 60 min) did not have a detrimental effect on the electrochemical behavior of $Ti_3C_2T_x$ modified GCE (Fig. 3 and Fig. S1). When $Ti_3C_2T_x$ modified GCE was exposed to potentials above 200 mV, it was possible to observe partial dissolution of the material from the modified GCE by a naked eye.

3.3. Raman spectra analysis

Results indicated that optimal power density for obtaining Raman spectra was 0.5 mW (Fig. S2) and an optimal sonication time was 1 min, in an agreement with results obtained from electrochemical assays. The Raman spectrum of $Ti_3C_2T_x$ modified GCE showing peaks at 200, 380 and 610 cm^{-1} (Fig. 4) is in an agreement with results obtained in a previous study [45].

Moreover, intensity of D-band (1,391 cm^{-1}) compared to G-band (1,596 cm^{-1}) is very low, in agreement with a previous study, as well [45]. When o$Ti_3C_2T_x$ was inspected by Raman spectroscopy the spectra looked very similar to Raman spectra of $Ti_3C_2T_x$, with the only difference i.e. presence of a well-developed D-band at 1,391 cm^{-1}, indicating induction of disorder within o$Ti_3C_2T_x$ (Fig. 4) [46]. Interestingly, in the Raman spectrum of oMXene a major peak at 144 cm^{-1} and other minor peaks observed at 394, 513 and 635 cm^{-1} (attributed to anatase TiO_2) [22,45] are not visible, indicating low density of anatase TiO_2 on the surface of o$Ti_3C_2T_x$.

3.4. Contact angle measurements

Contact angle measurements obtained using an Owens-Wendt-Rable-Kaeble model are summarized in Table S1. A decrease of contact angle in water (from 36° to 30°) and an increase of a polar component of a free surface energy (from 30 mJ m^{-2} to 35 mJ m^{-2}) for o$Ti_3C_2T_x$ compared to $Ti_3C_2T_x$ indicate that oxidation of the sample by LSV introduced polar functional groups into the sample of o$Ti_3C_2T_x$ or removed F^- groups making the surface of o$Ti_3C_2T_x$ more hydrophilic compared to $Ti_3C_2T_x$. The contact angle of 36° measured on $Ti_3C_2T_x$ is in an excellent agreement with a previous study showing a value of 34° [17]. Images from such measurements are shown in Fig. S3.

3.5. AFM measurements

AFM measurements were performed to see surface morphology of $Ti_3C_2T_x$ or o$Ti_3C_2T_x$ layers and results indicated a substantial decrease in the value of mean square roughness (R_q) for $Ti_3C_2T_x$with a value of 1.6 nm compared to o$Ti_3C_2T_x$modified interface with a value of 0.2 nm. Presence of either higher or deeper features on $Ti_3C_2T_x$interface compared to o$Ti_3C_2T_x$could be anticipated when looking on a parameter of image R_{max} (i.e. a value of 10.5 nm for $Ti_3C_2T_x$and a value of 1.4 nm for o$Ti_3C_2T_x$) (Table S2) [22]. Typical AFM images of $Ti_3C_2T_x$ and o$Ti_3C_2T_x$

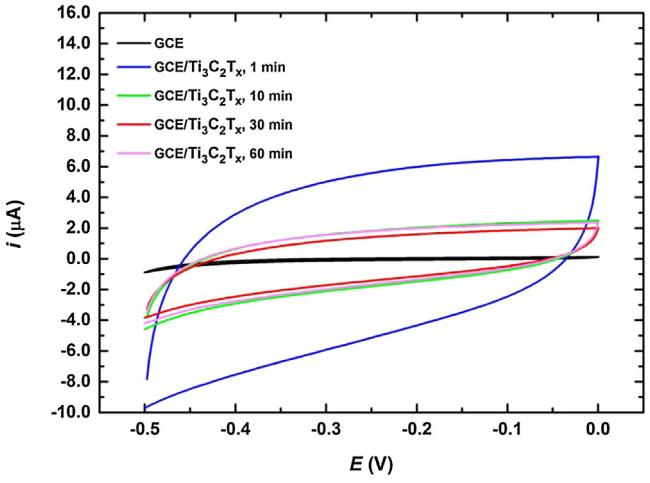

Fig. 3. CVs performed in 0.1 M PB pH 7.0 at bare GCE and at GCE/$Ti_3C_2T_x$ run at a scan rate of 100 mV s^{-1}. $Ti_3C_2T_x$dispersions deposited on GCE were prepared by sonication of the mixture for 1, 10, 30 or 60 min.

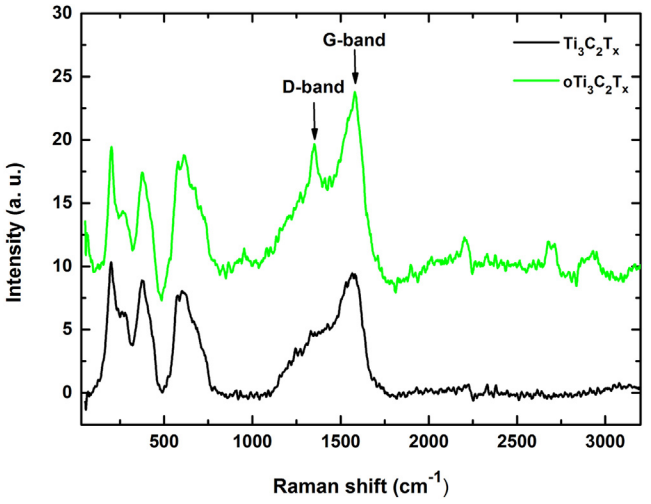

Fig. 4. Representative Raman spectra of $Ti_3C_2T_x$ and o$Ti_3C_2T_x$acquired with laser power set to 0.5 mW.

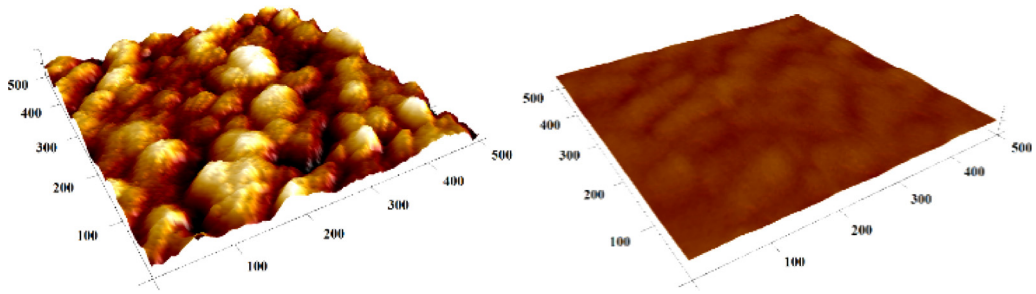

Fig. 5. Typical AFM image of $Ti_3C_2T_x$(left) and o$Ti_3C_2T_x$ (right) modified Au chip, showing rougher surface of $Ti_3C_2T_x$ compared to o$Ti_3C_2T_x$. In both cases z-axis was set to 11 nm.

modified gold chips are shown in Fig. 5. However, o$Ti_3C_2T_x$ modified gold surface is not completely flat as could be indicated from Fig. 5 **right**, but exhibits a moderate roughness (Fig. S4).

AFM height profile analysis of a more concentrated sample deposited compared to Fig. 5 revealed a decrease in $Ti_3C_2T_x$ film thickness (correlating with a decrease observed for R_q value) from (7.8 ± 0.8) nm to (2.2 ± 0.9) nm for o$Ti_3C_2T_x$, respectively. Moreover, layers of $Ti_3C_2T_x$ were clearly visible at the edge of each flake (as seen on Fig. S5 **left**). Thickness of these layers ranges from (0.9 ± 0.1) nm for o$Ti_3C_2T_x$ to (1.1 ± 0.1) nm for $Ti_3C_2T_x$, respectively, what correlates well with the previously published value for a Ti_3C_2X monolayer (1.0 ± 0.2) [47–49]. Average size of the isolated flakes on the surface was (123 ± 7) nm (correlating with the value of 100–200 nm range published previously) [50,51], as shown on Fig. S5 **right**, and the average surface density for the MXene films prepared was $\Gamma = (88 \pm 10)$ flakes μm^{-2} (2D projection of the 3D surface map).

3.6. XPS spectra

Analysis of both types of samples showed a significant decrease (from (18.8 ± 0.5) atomic % to (3.8 ± 1.7) atomic %) in F1 s content resulting in an increased hydrophilicity of o$Ti_3C_2T_x$ (Table S3, Fig. S6). The content of Ti decreased from (9.2 ± 0.1) atomic % for $Ti_3C_2T_x$ to (4.4 ± 3.2) atomic % for o$Ti_3C_2T_x$ (as shown in Fig. S6 **left**) with an increase of carbon content from (42.9 ± 0.3) atomic % for $Ti_3C_2T_x$ to (62.9 ± 5.7) atomic % for o$Ti_3C_2T_x$. The content of oxygen within both samples is approximately the same i.e. (29.2 ± 0.9) atomic % for $Ti_3C_2T_x$ or (29.0 ± 0.8) atomic % for o$Ti_3C_2T_x$. It is quite interesting to point out to the fact that measuring an atomic composition of $Ti_3C_2T_x$ by XPS was more reproducible with an average RSD of 1.9%, while an average RSD for measuring atomic composition of o$Ti_3C_2T_x$ was 32.3%, what can indicate more heterogeneous chemical and/or morphological composition of o$Ti_3C_2T_x$ surface compared to $Ti_3C_2T_x$.

3.7. XRD analysis

For all samples, two major XRD peaks were observed (see Fig. S7). One at $2\theta = 6.09 \pm 0.03°$ with calculated $\underline{d}$ lattice of 14.5 Å and an average domain size of 14 nm and the other one at $9.519 \pm 0.001°$ with calculated $\underline{d}$ lattice of 9.28 Å and an average domain size of 143.4 nm. The former peak indices disintegration of some larger particles into smaller ones with more distant individual sheets confirming that the performed sonication leads to an exfoliation of $Ti_3C_2T_X$ (see for example [17]). The former peak, on the other hand, revealed a presence of large particles (domain size of 143.4 nm, in agreement with AFM data discussed above) with smaller distance between individual sheets (i.e. 9.28 Å, again with agreement with AFM data discussed above), assigned most probably to the non-exfoliated material. This hypothesis is supported by a value of (11 ± 3) nm reported for particle size in 0001 direction for different MAXs after the HF treatment [11].

Besides the abovementioned two major peaks, small features at $19.107 \pm 0.004°$ were detected and a pattern with one peak at $38.780 \pm 0.004°$ and a second one at $38.876 \pm 0.003°$. Except for the first one, positions of all the peaks exhibited very narrow dispersions, suggesting that they should be assigned to crystallinity patterns which are not influenced by inevitable random variances in $Ti_3C_2T_X$ exfoliation and deposition steps. On the other side, the first peak is broad with a larger position values interval, suggesting that it originated from less regular structures, probably exfoliated $Ti_3C_2T_X$ sheets loosely stacked to each other via van der Walls or hydrophobic interactions. It should be also noted, that the difference between *d* parameters of particles represented by the two major peaks, i.e. 5.22 nm, is very close to the value reported by Lukatskaya et al. [52] for a lattice size change caused by intercalation of K^+ or NH_4^+ ion between $Ti_3C_2T_x$ sheets.

3.8. Secondary ion mass spectrometry (SIMS) analysis

SIMS is a technique for sensitive chemical surface analysis of samples [44]. In Fig. S8 and Fig. S9 there are shown representative mass spectra obtained for $Ti_3C_2T_x$ and o$Ti_3C_2T_x$ by SIMS. LSV procedure to prepare o$Ti_3C_2T_x$ was performed on $Ti_3C_2T_x$ deposited on bare Au chip (prepared by CVD method). In the mass spectrum of $Ti_3C_2T_x$ (Fig. S8) it was possible to see peaks, which were attributed to Ti^+ and TiO^+, but such peaks were not observed, when o$Ti_3C_2T_x$ was analyzed indicating most likely removal of an outer Ti layer from $Ti_3C_2T_x$ during exposure of $Ti_3C_2T_x$ to an anodic potential. A closer look at data presented in Fig. S8 showed an interesting fact that from $Ti_3C_2T_x$, ions of carbon with lower amount of oxygen (i.e. $C_{22}H_{29}O_2^+$, $C_{23}H_{31}O_2^+$ and $C_{24}H_{33}O_2^+$) were released and such ions could not be generated from o$Ti_3C_2T_x$ and that o$Ti_3C_2T_x$ contains highly oxidized carbon molecules indicated by presence of ions such as $C_{25}H_{25}O_4^+$, $C_{26}H_{27}O_4^+$ and $C_{27}H_{29}O_4^+$, which were not present in $Ti_3C_2T_x$ spectra. Furthermore, SIMS analysis revealed presence of F^- in the spectra acquired from $Ti_3C_2T_x$, while a peak attributed to presence of F^- ions in the spectra of o$Ti_3C_2T_x$ was less intensive in order of magnitude compared to $Ti_3C_2T_x$ (Fig. S10 and Fig. S11).

In Fig. S12 and Fig. S13 there are representative SIMS 2D images of fragments released from $Ti_3C_2T_x$ and o$Ti_3C_2T_x$ shown. Fragments detected in both samples (from upper left to middle right) are as follows: Li^+, CH_3^+, Na^+, $C_2H_5^+$, Ti^+ and Au^+. For bare $Ti_3C_2T_x$, isolated islets of Ti (10–20 μm) could be observed, in contrast to o$Ti_3C_2T_x$, where the Ti coverage is more uniform, however, with lower Ti intensity compared to $Ti_3C_2T_x$ (Fig. 6).

From all these characterization techniques we can make some conclusions: 1) from XPS and SIMS experiments it is clear that especially outer Ti containing layer of $Ti_3C_2T_x$ is influenced by application of an anodic voltage since SIMS image showed lower

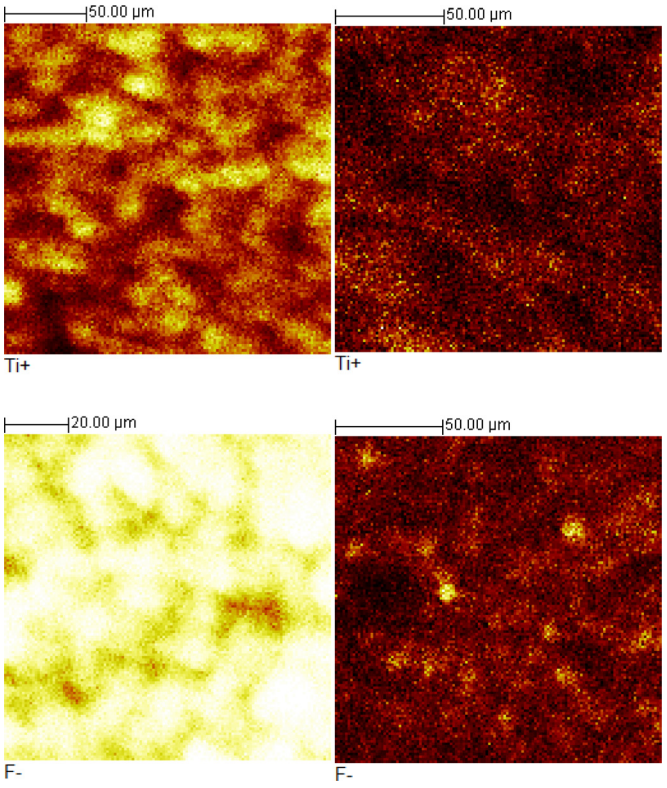

Fig. 6. SIMS 2D images for Ti^+ fragments of $Ti_3C_2T_x$ (left) and o$Ti_3C_2T_x$ (right) in a positive polarity (upper row) and SIMS 2D images for F^- fragments of $Ti_3C_2T_x$ (left) and o $Ti_3C_2T_x$ (right) in a negative polarity (lower row).

intensity of the upper Ti layer in the o$Ti_3C_2T_x$ sample compared to $Ti_3C_2T_x$, while XPS spectra with a laser beam reaching deeper into the o$Ti_3C_2T_x$ layer provided evidence about presence of Ti species in the sample of o$Ti_3C_2T_x$; 2) XPS measurements confirmed dramatic decrease of fluoride content from (18.8 ± 0.5) atomic % for $Ti_3C_2T_x$ to (3.8 ± 1.7) atomic % for o$Ti_3C_2T_x$ (Fig. S6 right) and SIMS experiments confirmed that the intensity of F^- ions is an order of magnitude lower in o$Ti_3C_2T_x$ sample compared to $Ti_3C_2T_x$ sample (Fig. S14 and Fig. S15), while F^- were present in $Ti_3C_2T_x$ sample (F^- peak area of 3,243,291 for $Ti_3C_2T_x$ and 284,426 for o$Ti_3C_2T_x$ with intensity of F^- peaks normalized to total ion intensity for both samples, as shown in Fig. 6); 3) dissolution of some material from GCE/$Ti_3C_2T_x$ during exposure to an anodic potential seen by a naked eye.

Based on these observations and using data already published in the literature we could propose the following equation behind oxidation of an outer layer of $Ti_3C_2T_x$ during exposure to an anodic potential:

$$Ti_3C_2F_x + 8H_2O \rightarrow 3TiO_2 + 2CO + 16H^+ + (16 - x)e^- + xF^- \quad (2)$$

When $Ti_3C_2F_x$ containing F^- ions is oxidized by the anodic potential it is oxidized to TiO_2 and most likely CO/CO_2 is emitted, an assumption based on oxidation of another type of MXene (i.e. Ti_2CT_x-based one) by H_2O_2 performed in DW [22]. After formation of TiO_2 on the outer layer of $Ti_3C_2F_x$ by an anodic applied voltage in presence of F^- ions a further step would be a dissolution of TiO_2 by forming a complex with F^- ions according to this equation [53]:

$$TiO_2 + 4H^+ + 6F^- \rightarrow [TiF_6]^{2-} + 2H_2O \quad (3)$$

This proposed mechanism explains both decrease of Ti and F^- content in the o$Ti_3C_2F_x$ sample as measured by XPS and SIMS. In a previous study formation of TiO_2 layer or TiO_2 islands on the surface of Ti_2CT_x MXene was observed, while exposing MXene to H_2O_2 in distilled water [22]. Since this reaction was performed in distilled water with concentration of H^+ ions too low, chemical etching via F^- ions destroying TiO_2 layer could not proceed (i.e. eqn. (3)). In the second study, formation of either rutile or anatase TiO_2 nanoparticles were formed on the surface of $Ti_3C_2T_x$ MXene by exposure to flash oxidation conditions (950 °C; 1 min) or to slow heating (450 °C; 2 h) [54]. This MXene sample equally as our $Ti_3C_2F_x$ sample contained F^- ions [54], but the main reasons why F^- did not dissolve forming TiO_2 nanoparticles in the previous study most likely was that high temperature applied effectively removed F^- ions, as suggested previously [18].

3.9. Electrochemical impedance spectroscopy (EIS) analysis

Using a R(Q[RW]) Randles equivalent circuit, the R_{ct} values obtained for bare GCE, $Ti_3C_2T_x$ modified GCE and o$Ti_3C_2T_x$modified GCE were (164 ± 36) Ω, (7,130 ± 600) Ω and (8,500 ± 1,000) Ω, respectively (Fig. 7), suggesting an increase of resistivity of o$Ti_3C_2T_x$ compared to $Ti_3C_2T_x$ indicating that o$Ti_3C_2T_x$is less conductive than o$Ti_3C_2T_x$.

3.10. Electrochemical oxidation of NADH

An interesting analyte applicable for proper function of enzyme-based biosensors is NADH, which is a byproduct of enzymatic action of dehydrogenases. There is a large anodic peak of NADH oxidation on $Ti_3C_2T_x$ modified GCE indicating a beneficial redox behavior of $Ti_3C_2T_x$ towards oxidation of NADH (Fig. 8). The onset potential for NADH oxidation is close to 200 mV, what is an attractive feature for potential construction of dehydrogenase-based biosensors operating with NADH as a cofactor and a value similar to the value obtained with the electrode modified by chemically reduced GO [55]. Oxidized $Ti_3C_2T_x$ exhibited much lower oxidation current of 23 µA (325 µA cm^{-2}, expressed *per* geometric surface area as usually described in the literature) compared to $Ti_3C_2T_x$ with a value of 144 µA (i.e., 2.04 mA cm^{-2}, both read at an applied potential of +780 mV) in presence of 2 mM NADH. A control experiment performed by oxidation of 2 mM NADH on GCE revealed a current of 32 µA, while a value of 19 µA (both read at a potential of 718 mV) was observed at GCE/o$Ti_3C_2T_x$ surface.

When CV experiment was performed with several scans, the experiment revealed that the beneficial redox behavior of $Ti_3C_2T_x$ substantially dropped in the 2nd scan and a further decrease of an

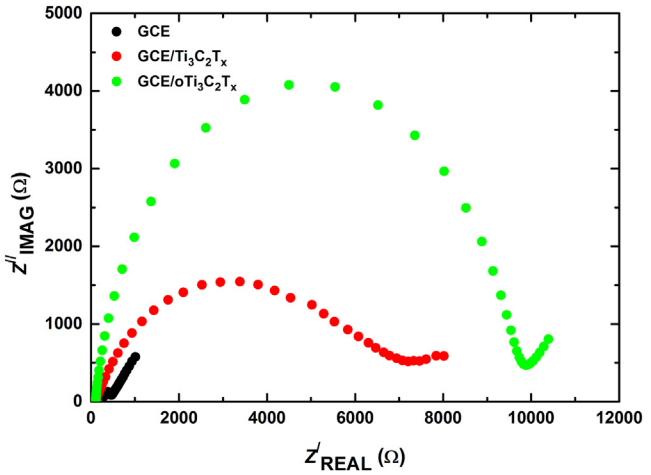

Fig. 7. Representative Nyquist plots at bare GCE, GCE/$Ti_3C_2T_x$ and GCE/o$Ti_3C_2T_x$ obtained in 5 mM ferricyanide/ferrocyanide solution in 0.1 M PB pH 7.0. For the assay 50 different frequencies in the range from 1.0 Hz to 10 kHz were applied.

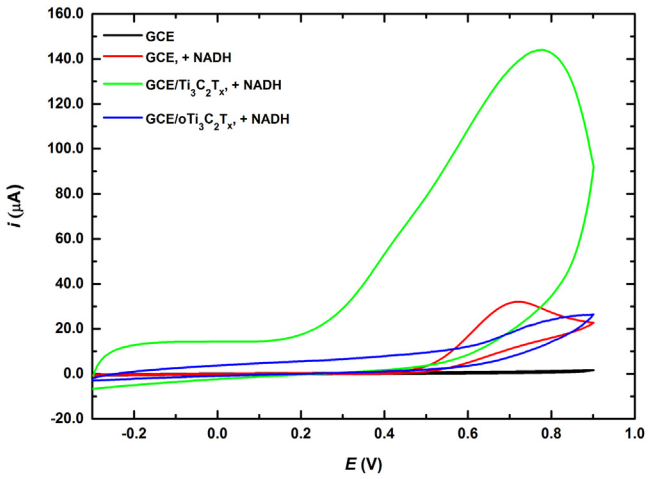

Fig. 8. CVs performed in 0.1 M PB pH 7.0 and in 2 mM NADH solution at bare GCE electrode and $Ti_3C_2T_x$ modified GCE run at a scan rate of 100 mV s^{-1}.

anodic current with an increased number of scans was observed (Fig. S16). Furthermore, chronoamperometric experiment (Fig. S17) confirmed that exposure of $Ti_3C_2T_x$ modified GCE to an anodic potential of 700 mV resulted in a decreased ability of $Ti_3C_2T_x$ modified GCE to oxidize NADH with the same current observed after 1 h on bare GCE and on $Ti_3C_2T_x$ modified GCE.

3.11. Oxygen reduction reaction (ORR)

From previous electrochemical investigations it was clear that $Ti_3C_2T_x$ modified GCE was possible to apply only for redox reactions, which occur in a cathodic potential window. This is why we tested performance of $Ti_3C_2T_x$ modified GCE for ORR and for reduction of H_2O_2, reactions, which can be applied for construction of sensors or biosensors. ORR is of high importance for many applications, e.g. hydrogen-oxygen fuel cells, metal-air batteries and biosensors, as well [56].

The results indicate that especially acidic environment i.e. 0.1 M H_2SO_4 is suitable for ORR to occur with a possibility to achieve a moderate current density in presence of oxygen and again it was confirmed that $oTi_3C_2T_x$ has only a limited ability to reduce oxygen compared to $Ti_3C_2T_x$ modified GCE (Fig. 9). The current density of 330 μA cm^{-2} (at −590 mV) for $oTi_3C_2F_x$ and current density of 500 μA cm^{-2} (at −590 mV) for $Ti_3C_2F_x$ were observed when CV assayed in presence of air were subtracted from CV obtained under N_2 atmosphere.

In an alkaline solution, subtracted CV for ORR measured in 0.1 M NaOH showed an onset potentials at −500 mV for $oTi_3C_2T_x$ and at −550 mV for $Ti_3C_2T_x$ with a maximal current density of 80 μA cm^{-2} for $oTi_3C_2T_x$ and 63 μA cm^{-2} for $Ti_3C_2T_x$. In a previous study an onset potential for ORR in 0.1 M NaOH of −450 mV and −700 mV was reported for graphene with a current density of 180 μA cm^{-2} using a rotating disc electrode (1,000 rpm) [57]. The same study showed that N-doped graphene showed an onset potential for ORR in 0.1 M NaOH of −200 mV with a limiting current density of ~800 μA cm^{-2} using a rotating disc electrode (1,000 rpm), while Pt/C electrode showed a limiting current density of ~220 μA cm^{-2} [57]. Furthermore, effectivity of ORR reaction can be enhanced by attachment of nanoparticles (i.e. Co nanoparticles) to N-doped graphene with an onset potential at −200 mV and a limiting current density of 4–5 mA cm^{-2} [58]. Thus, even though $oTi_3C_2T_x$ and $Ti_3C_2T_x$ without any further modifications are not as good catalysts for ORR in acidic and alkaline solutions as the best catalysts described in the literature (such are for example noble metal-free, nitrogen and sulphur co-doped graphene/carbon-nanotube material decorated with Co nanoparticles offering current density of ~7 mA cm^{-2} in alkaline and acidic media [59]), $Ti_3C_2T_x$ or $oTi_3C_2T_x$ could be a good substrate for accommodation of various types of nanoparticles for subsequent effective ORR reactions in both media. Additional possible application of $Ti_3C_2T_x$ to perform ORR is in construction of enzymatic biosensors using oxidases, which upon enzymatic action consume oxygen as a co-substrate [42] for analysis of a wide range of analytes.

3.12. Electrochemical reduction of H_2O_2

Reduction of H_2O_2 on $Ti_3C_2T_x$ modified electrode started with an onset potential of ~−160 mV, comparable to the results obtained on chemically reduced GO [55] or carbon nanotube modified electrode [60]. Thus, it can be concluded that $Ti_3C_2T_x$ modified electrodes could be applied in oxidase-based biosensing as effectively as graphene-based devices. The results indicated that H_2O_2 can be effectively reduced by $Ti_3C_2T_x$ modified GCE and less effective by $oTi_3C_2T_x$ modified GCE (Fig. S18). Moreover, intercalation of DMSO into $Ti_3C_2T_x$ during $Ti_3C_2T_x$ sonication resulted in a less effective redox behavior towards H_2O_2 reduction both for $Ti_3C_2T_x$ and $oTi_3C_2T_x$ modified GCE compared to GCE modified only by $Ti_3C_2T_x$ or $oTi_3C_2T_x$ without being intercalated with DMSO (Fig. S18). This is why we tested $Ti_3C_2T_x$ modified GCE as a sensor for detection of H_2O_2 at an applied potential of − 500 mV (Fig. 10).

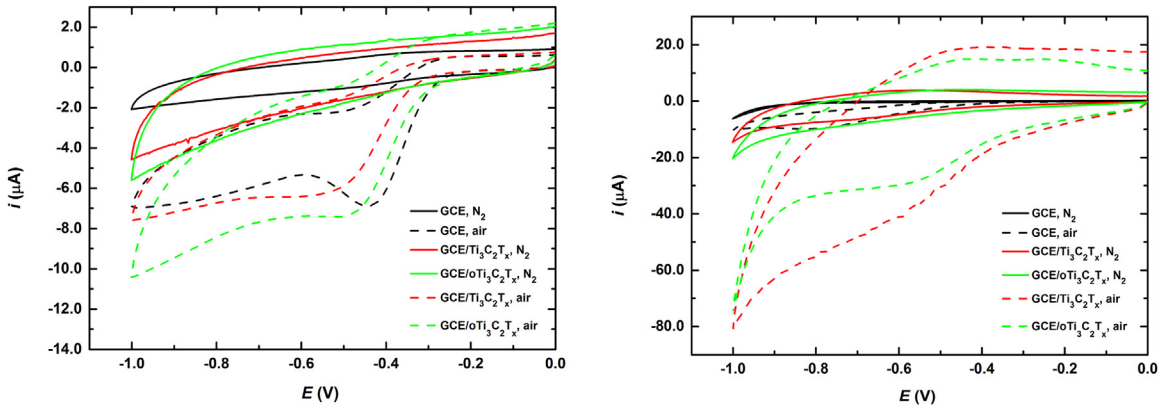

Fig. 9. CVs of ORR run at bare GCE, GCE/$Ti_3C_2T_x$ and GCE/$oTi_3C_2T_x$ in 0.1 M NaOH (left) or 0.1 M H_2SO_4 (right) under N_2 and air atmosphere. The experiments were run at a sweep rate of 100 mV s^{-1}.

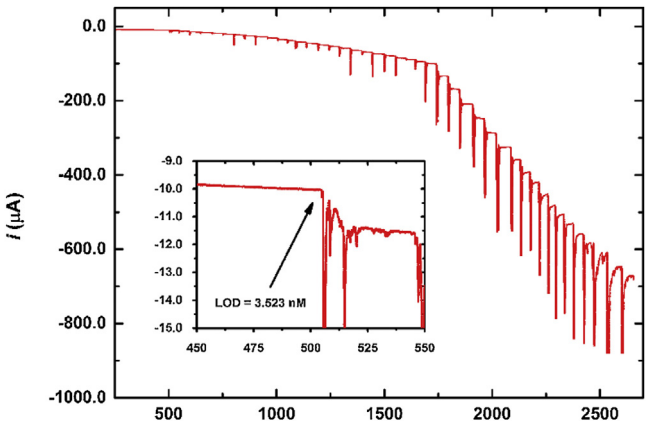

Fig. 10. Chronoamperogram recorded for $Ti_3C_2T_x$ modified rotating disc electrode (RDE) in 0.1 M PB pH 7.0 with H_2O_2 additions at a working potential of −0.5 V. Arrow in the inset picture shows the first addition of stock H_2O_2 solution. Limit of detection was calculated as S/N = 3 from the 1st H_2O_2 injection.

The noise of the sensor *prior* H_2O_2 addition was ~30 nA and if we apply S/N=3 for calculation of a limit of detection (LOD) then we could get LOD of 0.7 nM and if we take into account noise level of ~150 nA, after addition of H_2O_2, then we can calculate LOD as 3.5 nM (Fig. 10). The sensor towards H_2O_2 exhibited sensitivity of detection of 596 mA cm^{-2} mM^{-1} (Fig. S19). The response time for detection of H_2O_2 was ~10 s (Fig. 10). The H_2O_2 sensor based on $Ti_3C_2T_x$ is much more sensitive compared to previously published H_2O_2 sensors with sensitivity up to 1.08 mA mM^{-1} cm^{-2} and LOD down to 20 nM [61–64]. There are however some papers reporting similar sensitivity or lower detection limits. For example Prussian blue based nanoelectrode array could reductively detect H_2O_2 down to 10 nM with a sensitivity of 60 μA mM^{-1} cm^{-2} [65], Prussian blue at Pt nanoparticles and carbon felt could detect H_2O_2 down to 1.2 nM with a sensitivity of 41 mA mM^{-1} cm^{-2} [66], Au-Pt nanoparticle-modified ionic liquid composite electrode could reductively detect H_2O_2 down to 0.3 nM with a sensitivity of 3.98 mA mM^{-1} cm^{-2} [67] and 3D porous Prussian blue layer deposited on graphene nanocomposite could detect H_2O_2 down to 5 nM [68].

4. Conclusions

The study showed that exposure of $Ti_3C_2T_x$ to an anodic potential induces formation of TiO_2, which is subsequently most likely etched from the $Ti_3C_2F_x$ surface by present F^- ions. However, pristine $Ti_3C_2T_x$ could be effectively applied in a cathodic potential window for sensing purposes. Results suggested that $Ti_3C_2T_x$ exhibits low catalytic activity for ORR run either in acidic or alkaline media, but $Ti_3C_2T_x$ was proved as an excellent catalyst for reduction of H_2O_2, and the H_2O_2 sensor based on $Ti_3C_2T_x$ is the most sensitive device described so far with a detection limit of 0.7 nM comparable to the best device described so far (i.e. 0.3 nM) [67]. It is possible that further modification of $Ti_3C_2T_x$ by metallic nanoparticles could further enhance performance of modified $Ti_3C_2T_x$ to detect H_2O_2.

Acknowledgements

Financial support received from the Slovak Scientific Grant Agency VEGA 2/0090/16 and from the Slovak Research and Development Agency APVV 14-0753 is acknowledged. The research leading to these results received funding from the European Research Council under the European Union's Seventh Framework Program (FP/2007-2013)/ERC Grant Agreement no. 311532. This publication was made possible by NPRP grant no. 6-381-1-078 from the Qatar National Research Fund (a member of the Qatar Foundation). This publication is the result of the project implementation: Applied research in the field of industrial biocatalysis, ITMS code: 26240220079 supported by the Research & Development Operational Programme funded by the ERDF. Authors would like to thank prof. Yury Gogotsi for proving the sample of $Ti_3C_2T_x$ MXene and for his valuable comments regarding the manuscript.

Appendix A. Supplementary data

Supplementary data associated with this article can be found, in the online version, at http://dx.doi.org/10.1016/j.electacta.2017.03.073.

References

[1] C.R. Kagan, L.E. Fernandez, Y. Gogotsi, P.T. Hammond, M.C. Hersam, A.E. Nel, R. M. Penner, C.G. Willson, P.S. Weiss, Nano Day: Celebrating the Next Decade of Nanoscience and Nanotechnology, ACS Nano 10 (2016) 9093–9103.
[2] A.T.S. Wee, M.C. Hersam, M. Chhowalla, Y. Gogotsi, An Update from Flatland, ACS Nano 10 (2016) 8121–8123.
[3] B. Mendoza-Sánchez, Y. Gogotsi, Synthesis of Two-Dimensional Materials for Capacitive Energy Storage, Adv. Mater. 28 (2016) 6104–6135.
[4] F. Shahzad, M. Alhabeb, C.B. Hatter, B. Anasori, S. Man Hong, C.M. Koo, Y. Gogotsi, Electromagnetic interference shielding with 2D transition metal carbides (MXenes), Science 353 (2016) 1137–1140.
[5] K.S. Novoselov, A.K. Geim, S.V. Morozov, D. Jiang, Y. Zhang, S.V. Dubonos, I.V. Grigorieva, A.A. Firsov, Electric Field Effect in Atomically Thin Carbon Films, Science 306 (2004) 666–669.
[6] A. Pakdel, Y. Bando, D. Golberg, Nano boron nitride flatland, Chem. Soc. Rev. 43 (2014) 934–959.
[7] V. Sorkin, H. Pan, H. Shi, S.Y. Quek, Y.W. Zhang, Nanoscale Transition Metal Dichalcogenides: Structures, Properties, and Applications, Crit. Rev. Solid State Mater. Sci. 39 (2014) 319–367.
[8] J. Halim, K.M. Cook, M. Naguib, P. Eklund, Y. Gogotsi, J. Rosen, M.W. Barsoum, X-ray photoelectron spectroscopy of select multi-layered transition metal carbides (MXenes), Appl. Surf. Sci. 362 (2016) 406–417.
[9] D.R. Miller, S.A. Akbar, P.A. Morris, Nanoscale metal oxide-based heterojunctions for gas sensing: A review, Sens. Actuat. B: Chem. 204 (2014) 250–272.
[10] K. Zhang, X. Han, Z. Hu, X. Zhang, Z. Tao, J. Chen, Nanostructured Mn-based oxides for electrochemical energy storage and conversion, Chem. Soc. Rev. 44 (2015) 699–728.
[11] M. Naguib, M. Kurtoglu, V. Presser, J. Lu, J. Niu, M. Heon, L. Hultman, Y. Gogotsi, M.W. Barsoum, Two-Dimensional Nanocrystals Produced by Exfoliation of Ti3AlC2, Adv. Mater. 23 (2011) 4248–4253.
[12] B. Anasori, Y. Xie, M. Beidaghi, J. Lu, B.C. Hosler, L. Hultman, P.R.C. Kent, Y. Gogotsi, M.W. Barsoum, Two-Dimensional, Ordered: Double Transition Metals Carbides (MXenes), ACS Nano 9 (2015) 9507–9516.
[13] X. Xie, M.-Q. Zhao, B. Anasori, K. Maleski, C.E. Ren, J. Li, B.W. Byles, E. Pomerantseva, G. Wang, Y. Gogotsi, Porous heterostructured MXene/carbon nanotube composite paper with high volumetric capacity for sodium-based energy storage devices, Nano Energy 26 (2016) 513–523.
[14] X. Sang, Y. Xie, M.-W. Lin, M. Alhabeb, K.L. Van Aken, Y. Gogotsi, P.R.C. Kent, K. Xiao, R.R. Unocic, Atomic Defects in Monolayer Titanium Carbide (Ti3C2Tx) MXene, ACS Nano 10 (2016) 9193–9200.
[15] K. Wang, Y. Zhou, W. Xu, D. Huang, Z. Wang, M. Hong, Fabrication and thermal stability of two-dimensional carbide Ti3C2 nanosheets, Ceram. Int. 42 (2016) 8419–8424.
[16] M. Naguib, Y. Gogotsi, Synthesis of Two-Dimensional Materials by Selective Extraction, Acc. Chem. Res. 48 (2015) 128–135.
[17] M. Naguib, O. Mashtalir, J. Carle, V. Presser, J. Lu, L. Hultman, Y. Gogotsi, M.W. Barsoum, Two-Dimensional Transition Metal Carbides, ACS Nano 6 (2012) 1322–1331.
[18] H. Wang, Y. Wu, J. Zhang, G. Li, H. Huang, X. Zhang, Q. Jiang, Enhancement of the electrical properties of MXene Ti3C2 nanosheets by post-treatments of alkalization and calcination, Mater. Lett. 160 (2015) 537–540.
[19] Y. Xie, Y. Dall'Agnese, M. Naguib, Y. Gogotsi, M.W. Barsoum, H.L. Zhuang, P.R.C. Kent, Prediction and Characterization of MXene Nanosheet Anodes for Non-Lithium-Ion Batteries, ACS Nano 8 (2014) 9606–9615.
[20] D. Er, J. Li, M. Naguib, Y. Gogotsi, V.B. Shenoy, Ti3C2 MXene as a High Capacity Electrode Material for Metal (Li, Na, K, Ca) Ion Batteries, ACS Appl. Mater. Interf. 6 (2014) 11173–11179.
[21] X. Liang, A. Garsuch, L.F. Nazar, Sulfur Cathodes Based on Conductive MXene Nanosheets for High-Performance Lithium–Sulfur Batteries, Angew. Chem. Int. Ed. 54 (2015) 3907–3911.

[22] B. Ahmed, D.H. Anjum, M.N. Hedhili, Y. Gogotsi, H.N. Alshareef, H2O2 assisted room temperature oxidation of Ti2C MXene for Li-ion battery anodes, Nanoscale 8 (2016) 7580–7587.
[23] M. Ghidiu, J. Halim, S. Kota, D. Bish, Y. Gogotsi, M.W. Barsoum, Ion-Exchange and Cation Solvation Reactions in Ti3C2 MXene, Chem. Mater. 28 (2016) 3507–3514.
[24] A. Byeon, M.-Q. Zhao, C.E. Ren, J. Halim, S. Kota, P. Urbankowski, B. Anasori, M. W. Barsoum, Y. Gogotsi, Two-Dimensional Titanium Carbide MXene As a Cathode Material for Hybrid Magnesium/Lithium-Ion Batteries, ACS Appl. Mater. Interf. (2016), doi:http://dx.doi.org/10.1021/acsami.6b04198.
[25] K. Xu, X. Ji, B. Zhang, C. Chen, Y. Ruan, L. Miao, J. Jiang, Charging/Discharging Dynamics in Two-Dimensional Titanium Carbide (MXene) Slit Nanopore: Insights from molecular dynamic study, Electrochim. Acta 196 (2016) 75–83.
[26] R.B. Rakhi, B. Ahmed, M.N. Hedhili, D.H. Anjum, H.N. Alshareef, Effect of Postetch Annealing Gas Composition on the Structural and Electrochemical Properties of Ti2CTx MXene Electrodes for Supercapacitor Applications, Chem. Mater. 27 (2015) 5314–5323.
[27] X. Ji, K. Xu, C. Chen, B. Zhang, Y. Ruan, J. Liu, L. Miao, J. Jiang, Probing the electrochemical capacitance of MXene nanosheets for high-performance pseudocapacitors, Phys. Chem. Chem. Phys. 18 (2016) 4460–4467.
[28] X. Wang, S. Kajiyama, H. Iinuma, E. Hosono, S. Oro, I. Moriguchi, M. Okubo, A. Yamada, Pseudocapacitance of MXene nanosheets for high-power sodium-ion hybrid capacitors, Nat. Commun. 6 (2015) 6544.
[29] Q. Peng, J. Guo, Q. Zhang, J. Xiang, B. Liu, A. Zhou, R. Liu, Y. Tian, Unique Lead Adsorption Behavior of Activated Hydroxyl Group in Two-Dimensional Titanium Carbide, J. Am. Chem. Soc. 136 (2014) 4113–4116.
[30] K. Rasool, M. Helal, A. Ali, C.E. Ren, Y. Gogotsi, K.A. Mahmoud, Antibacterial Activity of Ti3C2Tx MXene, ACS Nano 10 (2016) 3674–3684.
[31] O. Mashtalir, K.M. Cook, V.N. Mochalin, M. Crowe, M.W. Barsoum, Y. Gogotsi, Dye adsorption and decomposition on two-dimensional titanium carbide in aqueous media, J. Mater. Chem. A 2 (2014) 14334–14338.
[32] F. Wang, C. Yang, C. Duan, D. Xiao, Y. Tang, J. Zhu, An Organ-Like Titanium Carbide Material (MXene) with Multilayer Structure Encapsulating Hemoglobin for a Mediator-Free Biosensor, J. Electrochem. Soc. 162 (2015) B16–B21.
[33] F. Wang, C. Yang, M. Duan, Y. Tang, J. Zhu, TiO2 nanoparticle modified organ-like Ti3C2 MXene nanocomposite encapsulating hemoglobin for a mediator-free biosensor with excellent performances, Biosens. Bioelectron. 74 (2015) 1022–1028.
[34] H. Liu, C. Duan, C. Yang, W. Shen, F. Wang, Z. Zhu, A novel nitrite biosensor based on the direct electrochemistry of hemoglobin immobilized on MXene-Ti3C2, Sens. Actuat. B: Chem. 218 (2015) 60–66.
[35] R. Rakhi, P. Nayuk, C. Xia, H.N. Alshareef, Novel amperometric glucose biosensor based on MXene nanocomposite, Sci. Rep. 6 (2016) 36422.
[36] X.-f. Yu, Y.-c. Li, J.-b. Cheng, Z.-b. Liu, Q.-z. Li, W.-z. Li, X. Yang, B. Xiao, Monolayer Ti2CO2: A Promising Candidate for NH3 Sensor or Capturer with High Sensitivity and Selectivity, ACS Appl. Mater. Interf. 7 (2015) 13707–13713.
[37] B. Xu, M. Zhu, W. Zhang, X. Zhen, Z. Pei, Q. Xue, C. Zhi, P. Shi, Ultrathin MXene-Micropattern-Based Field-Effect Transistor for Probing Neural Activity, Adv. Mater. 28 (2016) 3333–3339.
[38] X.M. Chen, G.H. Wu, Z.X. Cai, M. Oyama, X. Chen, Advances in enzyme-free electrochemical sensors for hydrogen peroxide, glucose, and uric acid, Microchim. Acta 181 (2014) 689–705.
[39] X.H. Liu, Z.H. Nan, Y. Qiu, L.C. Zheng, X.Q. Lu, Hydrophobic ionic liquid immoblizing cholesterol oxidase on the electrodeposited Prussian blue on glassy carbon electrode for detection of cholesterol, Electrochim. Acta 90 (2013) 203–209.
[40] E. Turkmen, S.Z. Bas, H. Gulce, S. Yildiz, Glucose biosensor based on immobilization of glucose oxidase in electropolymerized poly(o-phenylenediamine) film on platinum nanoparticles-polyvinylferrocenium modified electrode, Electrochim. Acta 123 (2014) 93–102.
[41] Y.L. Zhou, H.S. Yin, X.M. Meng, Z.N. Xu, Y.R. Fu, S.Y. Ai, Direct electrochemistry of sarcosine oxidase on graphene: chitosan and silver nanoparticles modified glassy carbon electrode and its biosensing for hydrogen peroxide, Electrochim. Acta 71 (2012) 294–301.
[42] J. Tkac, J.W. Whittaker, T. Ruzgas, The use of single walled carbon nanotubes dispersed in a chitosan matrix for preparation of a galactose biosensor, Biosens. Bioelectron. 22 (2007) 1820–1824.
[43] M.-Q. Zhao, C.E. Ren, Z. Ling, M.R. Lukatskaya, C. Zhang, K.L. Van Aken, M.W. Barsoum, Y. Gogotsi, Flexible MXene/Carbon Nanotube Composite Paper with High Volumetric Capacitance, Adv. Mater. (Weinheim, Ger.) 27 (2015) 339–345.
[44] L. Škantárová, A. Oriňák, R. Oriňáková, M. Jerigová, M. Stupavská, D. Velič, Functional silver nanostructured surfaces applied in SERS and SIMS, Surf. Interface Anal. 45 (2013) 1266–1272.
[45] M. Naguib, O. Mashtalir, M.R. Lukatskaya, B. Dyatkin, C. Zhang, V. Presser, Y. Gogotsi, M.W. Barsoum, One-step synthesis of nanocrystalline transition metal oxides on thin sheets of disordered graphitic carbon by oxidation of MXenes, Chem. Commun. 50 (2014) 7420–7423.
[46] T. Hu, J. Wang, H. Zhang, Z. Li, M. Hu, X. Wang, Vibrational properties of Ti3C2 and Ti3C2T2 (T = O, F: OH) monosheets by first-principles calculations: a comparative study, Phys. Chem. Chem. Phys. 17 (2015) 9997–10003.
[47] A. Lipatov, M. Alhabeb, M.R. Lukatskaya, A. Boson, Y. Gogotsi, A. Sinitskii, Effect of Synthesis on Quality, Electronic Properties and Environmental Stability of Individual Monolayer Ti3C2 MXene Flakes, Advanced Electronic Materials 2 (2016).
[48] A. Miranda, J. Halim, A. Lorke, M. Barsoum, Rendering Ti3C2T x (MXene) monolayers visible, Materials Research Letters (2017) 1–7.
[49] C.E. Ren, M. Zhao, T. Makaryan, J. Halim, M. Boota, S. Kota, B. Anasori, M.W. Barsoum, Y. Gogotsi, Porous Two-Dimensional Transition Metal Carbide (MXene) Flakes for High-Performance Li-Ion Storage, ChemElectroChem 3 (2016) 689–693.
[50] Z. Ling, C.E. Ren, M.-Q. Zhao, J. Yang, J.M. Giammarco, J. Qiu, M.W. Barsoum, Y. Gogotsi, Flexible and conductive MXene films and nanocomposites with high capacitance, Proceedings of the National Academy of Sciences 111 (2014) 16676–16681.
[51] A. Ali, A. Belaidi, S. Ali, M.I. Helal, K.A. Mahmoud, Transparent and conductive Ti3C2Tx (MXene) thin film fabrication by electrohydrodynamic atomization technique, Journal of Materials Science: Materials in Electronics 27 (2016) 5440–5445.
[52] M.R. Lukatskaya, O. Mashtalir, C.E. Ren, Y. Dall'Agnese, P. Rozier, P.L. Taberna, M. Naguib, P. Simon, M.W. Barsoum, Y. Gogotsi, Cation intercalation and high volumetric capacitance of two-dimensional titanium carbide, Science 341 (2013) 1502–1505.
[53] S. Huang, W. Peng, C. Ning, Q. Hu, H. Dong, Nanostructure Transition on Anodic Titanium: Structure Control via a Competition Strategy between Electrochemical Oxidation and Chemical Etching, J. Phys. Chem. C 116 (2012) 22359–22364.
[54] H. Ghassemi, W. Harlow, O. Mashtalir, M. Beidaghi, M.R. Lukatskaya, Y. Gogotsi, M.L. Taheri, In situ environmental transmission electron microscopy study of oxidation of two-dimensional Ti3C2 and formation of carbon-supported TiO2, J. Mater. Chem. A 2 (2014) 14339–14343.
[55] M. Zhou, Y. Zhai, S. Dong, Electrochemical Sensing and Biosensing Platform Based on Chemically Reduced Graphene Oxide, Anal. Chem. 81 (2009) 5603–5613.
[56] E.P. Randviir, C.E. Banks, The Oxygen Reduction Reaction at Graphene Modified Electrodes, Electroanalysis 26 (2014) 76–83.
[57] L. Qu, Y. Liu, J.-B. Baek, L. Dai, Nitrogen-doped graphene as efficient metal-free electrocatalyst for oxygen reduction in fuel cells, ACS Nano 4 (2010) 1321–1326.
[58] G. Zhang, W.T. Lu, F.F. Cao, Z.D. Xiao, X.S. Zheng, N-doped graphene coupled with Co nanoparticles as an efficient electrocatalyst for oxygen reduction in alkaline media, J. Power Sources 302 (2016) 114–125.
[59] V. Vij, J.N. Tiwari, K.S. Kim, Covalent versus Charge Transfer Modification of Graphene/Carbon-Nanotubes with Vitamin B1: Co/N/S-C Catalyst toward Excellent Oxygen Reduction, ACS Appl. Mater. Interf. 8 (2016) 16045–16052.
[60] J. Tkac, T. Ruzgas, Dispersion of single walled carbon nanotubes. Comparison of different dispersing strategies for preparation of modified electrodes toward hydrogen peroxide detection, Electrochem. Commun. 8 (2006) 899–903.
[61] M.H. Yeh, Y.S. Li, G.L. Chen, L.Y. Lin, T.J. Li, H.M. Chuang, C.Y. Hsieh, S.C. Lo, W.H. Chiang, K.C. Hoa, Facile Synthesis of Boron-doped Graphene Nanosheets with Hierarchical Microstructure at Atmosphere Pressure for Metal-free Electrochemical Detection of Hydrogen Peroxide, Electrochim. Acta 172 (2015) 52–60.
[62] W.N. Xu, J.L. Liu, M.J. Wang, L. Chen, X. Wang, C.G. Hu, Direct growth of MnOOH nanorod arrays on a carbon cloth for high-performance non-enzymatic hydrogen peroxide sensing, Anal. Chim. Acta 913 (2016) 128–136.
[63] Y. Pan, Z.H. Hou, H. Yang, Y.N. Liu, Hierarchical architecture of nanographene-coated rice-like manganese dioxide nanorods/graphene for enhanced electrocatalytic activity toward hydrogen peroxide reduction, Mater. Sci. Semicond. Process. 40 (2015) 176–182.
[64] W. Chen, S. Cai, Q.-Q. Ren, W. Wen, Y.-D. Zhao, Recent advances in electrochemical sensing for hydrogen peroxide: a review, Analyst 137 (2012) 49–58.
[65] A.A. Karyakin, E.A. Puganova, I.A. Budashov, I.N. Kurochkin, E.E. Karyakina, V.A. Levchenko, V.N. Matveyenko, S.D. Varfolomeyev, Prussian blue based nanoelectrode arrays for H2O2 detection, Anal. Chem. 76 (2004) 474–478.
[66] L. Han, S. Tricard, J. Fang, J. Zhao, W. Shen, Prussian blue @ platinum nanoparticles/graphite felt nanocomposite electrodes: Application as hydrogen peroxide sensor, Biosens. Bioelectron. 43 (2013) 120–124.
[67] F. Xiao, F. Zhao, Y. Zhang, G. Guo, B. Zeng, Ultrasonic Electrodeposition of Gold-Platinum Alloy Nanoparticles on Ionic Liquid-Chitosan Composite Film and Their Application in Fabricating Nonenzyme Hydrogen Peroxide Sensors, J. Phys. Chem. C 113 (2009) 849–855.
[68] L. Chen, X. Wang, X. Zhang, H. Zhang, 3D porous and redox-active Prussian blue-in-graphene aerogels for highly efficient electrochemical detection of H2O2, J. Mater. Chem. 22 (2012) 22090–22096.